

Nitrogen-Superdoped 3D Graphene Networks for High-Performance Supercapacitors

Weili Zhang, Chuan Xu, Chaoqun Ma, Guoxian Li, Yuzuo Wang, Kaiyu Zhang, Feng Li, Chang Liu, Hui-Ming Cheng, Youwei Du, Nujang Tang,* and Wencai Ren*

An N-superdoped 3D graphene network structure with an N-doping level up to 15.8 at% for high-performance supercapacitor is designed and synthesized, in which the graphene foam with high conductivity acts as skeleton and nested with N-superdoped reduced graphene oxide aerogels. This material shows a highly conductive interconnected 3D porous structure (3.33 S cm^{-1}), large surface area ($583 \text{ m}^2 \text{ g}^{-1}$), low internal resistance (0.4Ω), good wettability, and a great number of active sites. Because of the multiple synergistic effects of these features, the supercapacitors based on this material show a remarkably excellent electrochemical behavior with a high specific capacitance (of up to 380, 332, and 245 F g^{-1} in alkaline, acidic, and neutral electrolytes measured in three-electrode configuration, respectively, 297 F g^{-1} in alkaline electrolytes measured in two-electrode configuration), good rate capability, excellent cycling stability (93.5% retention after 4600 cycles), and low internal resistance (0.4Ω), resulting in high power density with proper high energy density.

Supercapacitors (SCs) are an important class of electrochemical energy storage devices with many advantages such as fast charging–discharging rates, high power density, and long cycle lifetime, because they store and release electrical energy based on the electrostatic interactions between ions in the electrolyte and electrodes.^[1–3] In general, an ideal electrode material for SCs should have good electrical conductivity, high surface area, and well wettability. Owing to the superior electrical conductivity and large specific surface area, graphene has attracted an extensive attention for SC applications.^[4–6] However, the 2D structure makes graphene sheets tend to aggregate during the fabrication process, which greatly decreases the specific surface area, causes inferior ions transport capabilities, and renders a substantial number of active sites inaccessible to reactants.^[7–10]

Dr. W. L. Zhang, Dr. K. Y. Zhang, Prof. Y. W. Du, Prof. N. J. Tang
National Laboratory of Solid State Microstructures
Collaborative Innovation Center of Advanced Microstructures
Jiangsu Provincial Key Laboratory for Nanotechnology
Nanjing University
Nanjing 210093, P. R. China
E-mail: tangnujiang@nju.edu.cn

Dr. C. Xu, Dr. C. Q. Ma, Dr. G. X. Li, Dr. Y. Z. Wang, Prof. F. Li,
Prof. C. Liu, Prof. H.-M. Cheng, Prof. W. C. Ren
Shenyang National Laboratory for Materials Science
Institute of Metal Research
Chinese Academy of Sciences
Shenyang 110016, P. R. China
E-mail: wcren@imr.ac.cn

DOI: 10.1002/adma.201701677

One way to solve this problem is to make hybrids using graphene and nanoparticles of high capacitance materials used for pseudocapacitors such as metals and metal oxides, which show greatly improved capacity, rate capability, and cycling stability because of the synergistic effect between graphene and nanoparticles.^[11–13] Alternatively, various 3D porous graphene materials such as foams, hydrogels, and sponges have been intensively developed to efficiently prevent the aggregation of graphene sheets to improve the performance of SCs.^[14–23] However, 3D porous graphene with both high surface area and high conductivity is difficult to be synthesized.^[24]

Graphene foam (GF) is a porous graphene macrostructure with 3D interconnected networks of high-quality graphene, which is prepared by chemical vapor deposition (CVD) method with metal foams as substrate. This material has both high electrical conductivity and large specific surface area, providing a great potential for SC applications.^[15,25,26] Unfortunately, the direct use of GF in SCs is limited because of the poor wettability with electrolyte, small surface area, and the lack of active sites. Although graphene hydrogels or sponges assembled by graphene oxide (GO) have much higher surface area and good wettability, they still suffer from low electrical conductivity and the number of active sites need to be improved as well. Recently, numerous studies have shown that N-doping of graphene can not only improve the wettability and the accessibility of the active surface area to the electrolyte solution as well as the binding with ions, but also improve the electrical conductivity by enriching the free charge-carrier density. As a result, SCs with N-doped graphene show comparable capacitances to those of pseudocapacitors (e.g., polymers, metal oxides) but keep the excellent cycling lifetime.^[21,27–30] However, N-doping of GF is very difficult because GF has perfect crystal lattice but N-doping mainly occurs at the vacancies of graphene sheets.^[31] Moreover, the doping level is usually very low (less than 10 at%) even for the GO or reduced GO (rGO) with many defects and vacancies.^[27,32,33] Fortunately, we have shown that rGO can be superdoped with N via fluorination by ammonia, and the N-doping level of N-superdoped rGO (NG) can reach high up to 30 at%.^[34] In addition, this superdoping method was predicted to be very useful for graphene materials in energy storage applications.^[35]

Here, we report an N-superdoped 3D graphene network structure (3D GF-NG) with an N-doping level up to 15.8 at%

for high-performance SCs, in which the GF with high conductivity acts as skeleton and nested with N-superdoped rGO aerogels (NG). This material combines the advantages of GF, rGO hydrogels, and high-level N-doping for SC applications, which has a highly conductive interconnected 3D porous structure, large surface area, low internal resistance, good wettability, and a great number of active sites. As a result, the supercapacitors based on this material show a remarkably excellent electrochemical behavior with a high specific capacitance (of up to 380, 332, and 245 F g⁻¹ in alkaline, acidic, and neutral electrolytes measured in three-electrode configuration, respectively, 297 F g⁻¹ in alkaline electrolytes measured in two-electrode

configuration), good rate capability, excellent cycling stability (93.5% retention after 4600 cycles), and low internal resistance (0.4 Ω), resulting in high power density with proper high energy density.

Figure 1a illustrates the fabrication of N-superdoped 3D graphene network structure. We first synthesized GF-rGO aerogel hybrid networks by immersing highly conductive GF with a 3D interconnected network structure and pore size of hundreds micrometers (Figure 1b) into aqueous solution of GO sheets (Figure 1c) followed by thermal annealing in Ar.^[36] This hybrid material not only remains the porous and interconnected network structure, but also enables N-doping

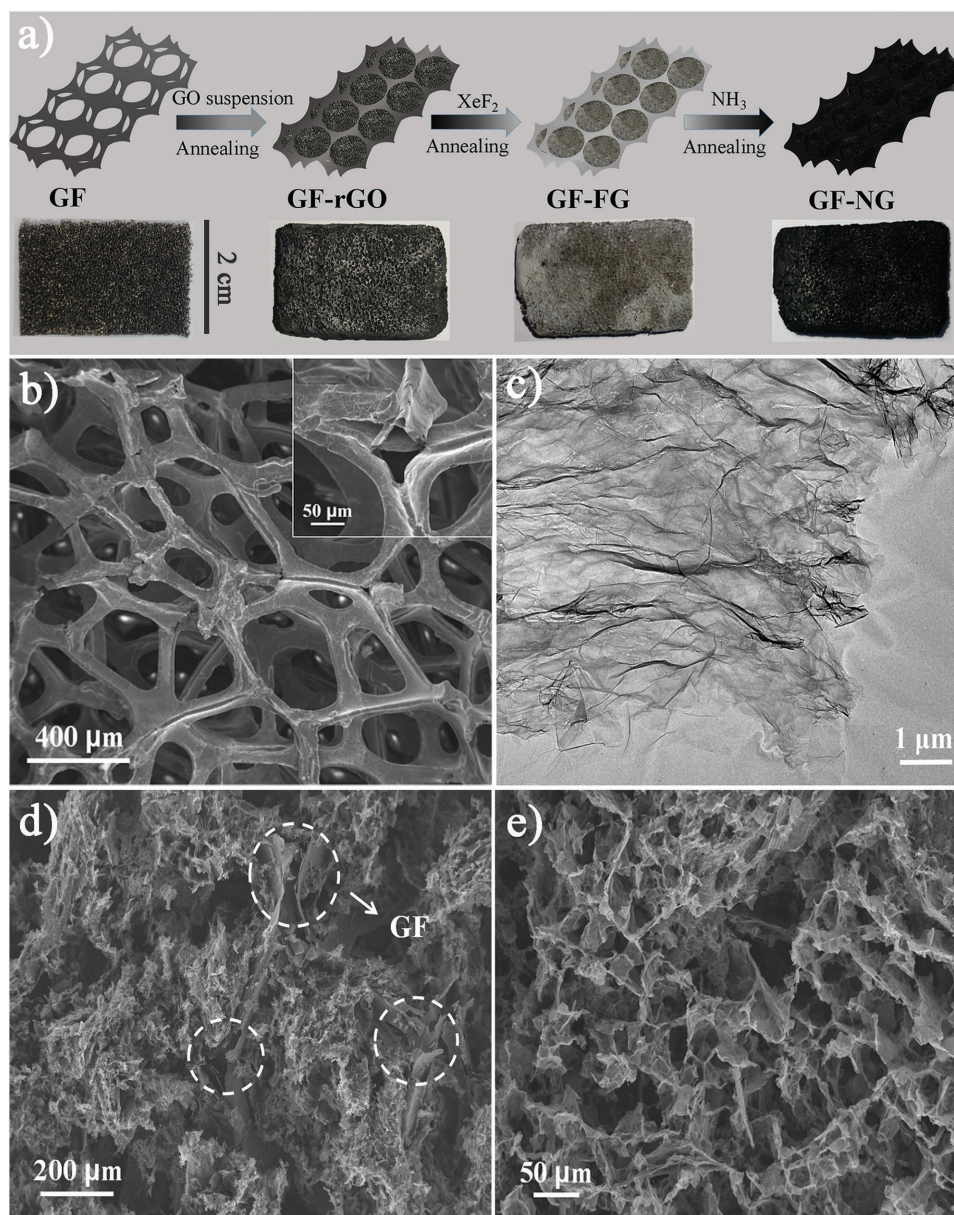


Figure 1. a) Schematic of the procedure for fabricating 3D GF-NG network macrostructure and the corresponding materials obtained at each step shown below. b) Field emission scanning electron microscope (FESEM) images of GF framework. Inset: high-magnification FESEM image. c) Transmission electron microscope (TEM) image of GO. d) Low-magnification and e) high-magnification cross-sectional FESEM images of GF-NG. The sections marked by dots circles are the skeletons of GF.

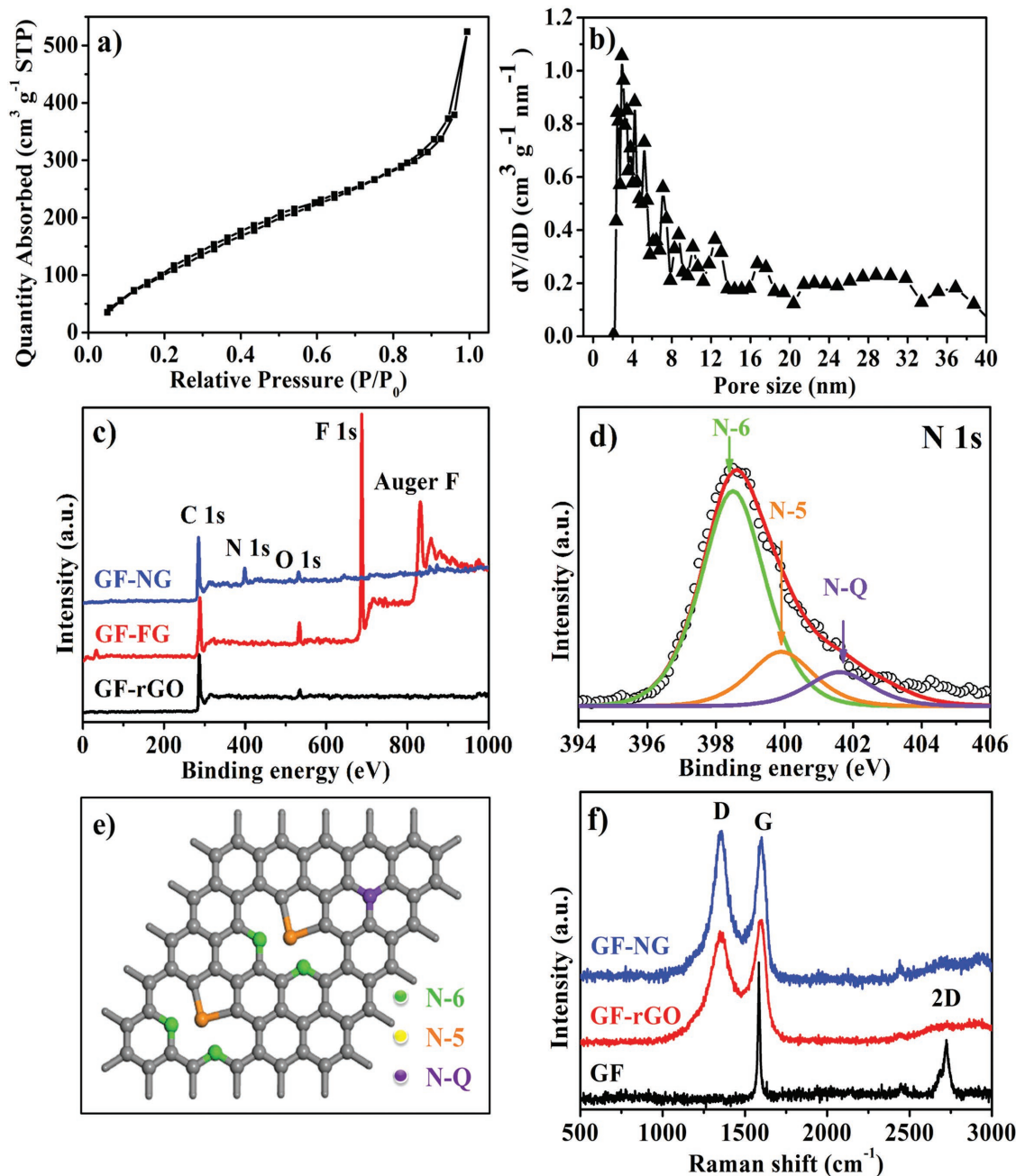


Figure 2. a) N_2 adsorption–desorption isotherms of GF-NG. b) Pore size distributions of GF-NG. c) XPS spectra over a wide range of binding energies of GF-rGO, GF-FG, and GF-NG. d) The fine-scanned N 1s spectrum of GF-NG. The dots are the measured data and the solid lines are the fitted curves. e) Schematic representation of NG. f) Raman spectra of GF, GF-rGO, and GF-NG.

because of the presence of defects and functional groups in GO sheets. Then, the GF-rGO aerogel hybrid networks were subjected to fluorination by annealing in Xenon difluoride (XeF_2). As reported previously, the fluorination followed by thermal defluorination can generate a high concentration of defects in GO, which stimulate N-doping of GO. After that, the obtained fluorinated GF-rGO (GF-FG) aerogel network was subjected to thermal annealing in ammonia for N-doping.^[34] The mass loading of NG in the GF-NG network was measured to be $\approx 1.0 \text{ mg cm}^{-2}$. As shown in Figure 1d,e

and Figures S1 and S2 (Supporting Information), the N-doped GO aerogels closely connected with the GF skeleton, forming an interconnected GF-NG network structure with a pore size ranging from several to dozens of micrometers. N_2 adsorption–desorption measurements show that GF-NG has a large specific surface area of $583 \text{ m}^2 \text{ g}^{-1}$ (Figure 2a), which is much higher than those of the ice-templated N-rGO ($190 \text{ m}^2 \text{ g}^{-1}$), graphene aerogel deposited on nickel foam ($463 \text{ m}^2 \text{ g}^{-1}$), and 3D N-doped graphene foam ($346 \text{ m}^2 \text{ g}^{-1}$).^[37–39] Moreover, it is clear that GF-NG possesses a large number of mesopores, most

of which are ranging from 2 to 10 nm (Figure 2b). It is known that rich mesopores can favor the infiltration of the electrode material and improve the surface usage. Therefore, the porous structure of GF-NG network ensures the large surface area and is favorable for rapid diffusion of electrolyte.^[40]

X-ray photoelectron spectroscopy (XPS) was used to characterize the chemical composition of the GF-rGO, GF-FG, and GF-NG networks. Based on the XPS results, the oxygen content (defined as O/C × 100 at%), fluorination degree (defined as F/C × 100 at%), and N-doping level (defined as N/C × 100 at%) can be calculated. As shown in Figure 2c and Figure S4 (Supporting Information), GF-rGO has a low oxygen content of 6.93 at%; after fluorination, a prominent F 1s peak appears, and the fluorination degree is 102.5 at%; after N-doping, the F 1s peak disappears almost completely and an extra N 1s peak appears, indicating complete defluorination and N-doping. It is worth noting that the N-doping level in GF-NG aerogel hybrid network is as high as ≈15.8 at%, which is much higher than those of reported N-doped rGO (typically less than 10 at%) fabricated by simple annealing without prefluorination.^[27,32,33] We also recorded the elemental mappings by using energy-dispersive spectrometer (EDS). It is important to note that nitrogen atoms are uniformly distributed in the GF-NG network (Figure S7, Supporting Information). To identify the N-doping structure, we performed fine scan of the N 1s XPS spectrum of GF-NG. As shown in Figure 2d, it can be deconvoluted into three subpeaks located at ≈398.5, 400, and 401.6 eV, which are, respectively, attributed to pyridinic N (N-6), pyrrolic N (N-5), and graphitic-like N (N-Q) (Figure 2e).^[34,41] Obviously, N-6 and N-5 dominate the N-doping in our hybrid networks.

It should be noted that the GF in the hybrid network is only weakly fluorinated and consequently doped with a low N-doping level of 1.05 at% because of its perfect crystal lattice (Figure S6, Supporting Information). Therefore, it retains its original high electrical conductivity as the skeletons of the 3D GF-NG networks. In contrast, the nested rGO aerogels are deeply fluorinated because of the presence of many defects and residual oxygen-containing functional groups, leading to a high N-doping level. They can be further confirmed by the Raman spectrum (Figure 2f). For GF, the intensity ratio of G band at 1590 cm⁻¹ and 2D band at 2722 cm⁻¹ reveal a few-layered structure of the GF, which benefits a good mechanical strength and highly conductive network.^[42,43] Moreover, compared to GF-rGO, GF-NG has a higher intensity ratio of D to G band, suggesting that more defects were introduced after N-superdoping. In addition, we found that the dispersibility of NG powder is much worse than that of GO (Figure S3a, Supporting Information), and the filling effect ratio of GF-NG by directly filling GF with NG via immersing the GF in NG solution (Figure S3b, Supporting Information) is much lower than that of GF-NG via immersing GF in GO solution, confirming that the immersion first and the N-doping next is more effective for fabricating N-superdoped 3D graphene networks.

It is well known that N-6 and N-Q bond with two and three sp² C atoms, respectively, and can contribute one pair of electrons to the conductive π-system (Figure 2e). As a consequence, both of them introduce one more electron to the system and, thus can be expected to greatly enhance the conductivity of

rGO sheets.^[27,34,44–46] Therefore, the GF-NG aerogel hybrid network constructs a highly conductive pathway for electron transport, which can enhance the rate performance of supercapacitors with high power density.^[18,24] The electrical conductivity of GF-NG network measured by four-point probe method is 3.33 S cm⁻¹, which is higher than that of GF-rGO (2.86 S cm⁻¹),^[36] indicative of the improved conductivity of GF-NG network. More importantly, the high-level and uniformly distributed N atoms provide GF-NG with both high-concentration active sites and good wettability. Besides, the N-Q groups can promote its interaction with the anions in the electrolyte and the formation of the electrical double layer, contributing to the high capacitance.^[27,47] Importantly, the GF can directly serve as the current collector, enabling the fabrication of binder-free supercapacitor. Therefore, together with the highly porous, conductive, and N-enriched structure mentioned above, this GF-NG aerogel hybrid network material is expected to be a good candidate for high-performance SCs.

The performances of the GF-NG as an electrode material for SCs were first investigated using cycle voltammetry (CV) and galvanostatic charge–discharge (GCD) with three-electrode configuration in 6.0 M KOH electrolyte. Figure 3a and Figure S9a (Supporting Information) display the CV curves for the potential from 0 to –0.8 V versus Ag/AgCl at scan rates ranging from 5 to 800 mV s⁻¹. It is found that all curves exhibit quasi-rectangular shapes, showing the behavior of an electrical double-layer capacitor. At a scan rate of 5 mV s⁻¹, a high capacitance of 312 F g⁻¹ is achieved (Figure S9b, Supporting Information). Even at a high scan rate of 800 mV s⁻¹, the CV curve is still close to rectangular with a capacitance of 160 F g⁻¹ (Figure S9b, Supporting Information), indicating a high rate capability and a low internal resistance. The GCD curves measured at different current densities from 0.6 to 80 A g⁻¹ show good symmetry and nearly linear discharge slopes (Figure 3b and Figure S10a, Supporting Information), implying the feature of electrical double-layer capacitor as well. Moreover, no obvious voltage drop appears, illustrating the low internal resistance of the electrode.

It should be noted that the capacitance of GF-rGO is only 75 F g⁻¹ under the scan rate of 5 mV s⁻¹ (Figure 3c, Figures S8 and S10b, Supporting Information). Surprisingly, after N-superdoping, the capacitance significantly increases to 312 F g⁻¹ under the same scan rate. For comparison, we also synthesized two other GF-NG samples with low N-doping levels (GF-NG-5.46 and GF-NG-8.94, the numbers denote the N-doping levels) by decreasing the fluorination degree of GF-FG (Figures S5 and S11 and Table S1, Supporting Information). The performances of GF-NGs with different N-doping levels clearly show that the higher the N-doping level, the better the performance (Figure 3c,d and Figure S10b, Supporting Information). All these results suggest that the N-superdoping significantly improves the capacitance of GF-NG. In addition, it is worth noting that the capacitance of GF-NG at 5 mV s⁻¹ (312 F g⁻¹) is much higher than that of NG powder (218 F g⁻¹) without GF with the same N-doping level at the same scan rate,^[34] indicating the important role of the porous and conductive network structure in the enhancement of specific capacitance. More importantly, the capacitance of GF-NG (312 F g⁻¹) is also much higher than the sum of those of GF (10 F g⁻¹) and NG (218 F g⁻¹) under the

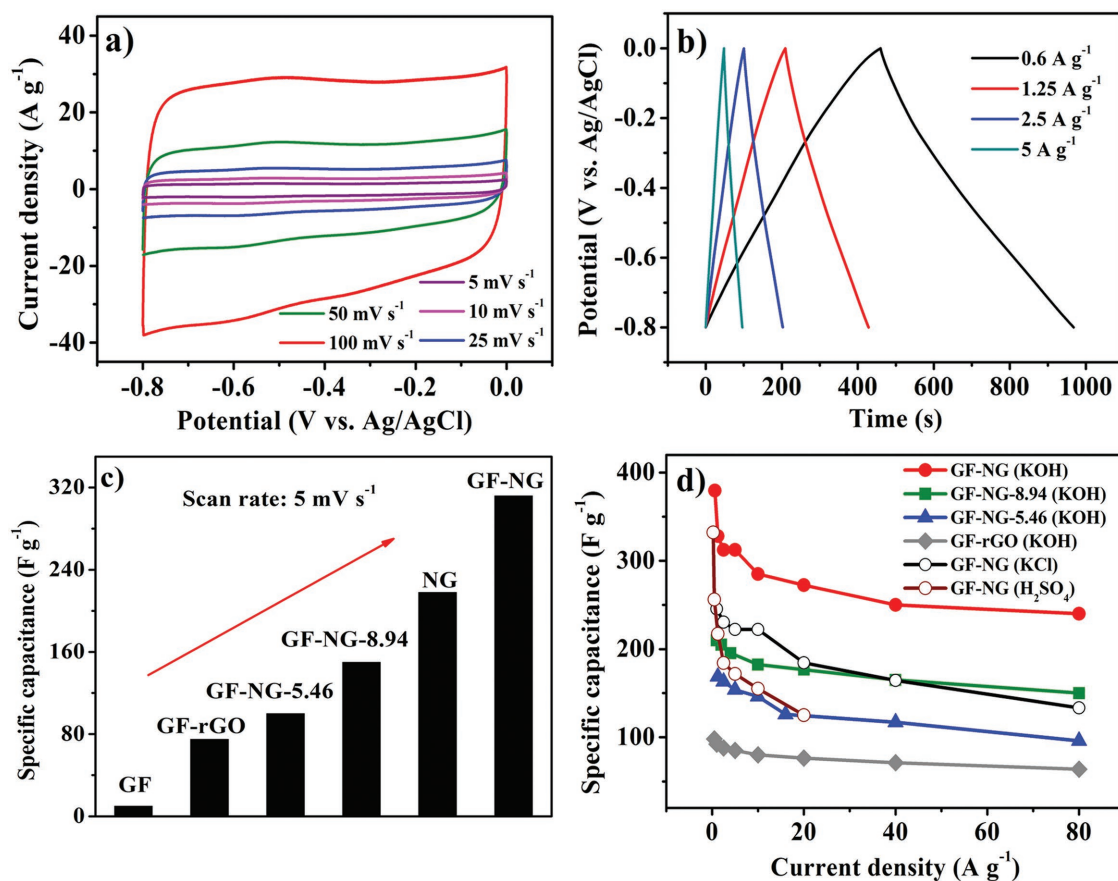


Figure 3. Electrochemical performances of GF-NG measured in three-electrode configuration. a) CV curves at scan rates from 5 to 100 mV s⁻¹ measured in 6.0 M KOH for GF-NG. b) GCD curves under different constant currents in 6.0 M KOH for GF-NG. c) The specific capacitance of GF, GF-rGO, GF-NGs, and NG powder calculated by the CV curves at 5 mV s⁻¹. d) The specific capacitance of GF-rGO and GF-NGs calculated at various current densities in 6.0 M KOH, 1.0 M KCl, and 1.0 M H₂SO₄.

same scan rate (Figure 3c). This further shows that constructing 3D GF-N-superdoped graphene networks provides us a rational design for the realization of SCs with excellent performance.

Figure 3d shows the capacitances for different current densities based on the slopes of the discharge curves. It can be found that the specific capacitance of GF-NG electrode reaches ≈ 380 F g⁻¹ at a current density of 0.6 A g⁻¹. Even at a high current density of 80 A g⁻¹, the value remains 240 F g⁻¹, which maintains 63.2% retention of the specific capacitance measured at 0.6 A g⁻¹. Furthermore, with the increase of the current density, the specific capacitance slowly decreases, demonstrative of high rate capability of GF-NG electrode. By fitting and calculating the capacitance and scan rate/discharge time from both the CV and GCD curves,^[37,48] it is found that at least about 80% of the capacitance comes from the electrical double-layer capacitance. For comparison, two other GF-NG samples with lower mass loading of NG (0.8 and 0.6 mg cm⁻²) were also synthesized. They show capacitances of 330 and 319 F g⁻¹, respectively (Figure S12, Supporting Information), which are clearly lower than that (380 F g⁻¹) of the GF-NG sample with a high mass loading of 1.0 mg cm⁻² (Figure S13, Supporting Information). Moreover, when GF-NG was tested in 1.0 M H₂SO₄ and 1.0 M KCl electrolyte, the capacitance values of GF-NG are up to 332 (0.25 A g⁻¹) and 245 F g⁻¹ (1 A g⁻¹) (Figure 3d and Figure S14, Supporting

Information). As listed in Table S2 (Supporting Information), it is clear that these performances tested in different electrolytes are better than those of other N-based materials, especially the performance tested in the KOH electrolyte.

To better illustrate the practical performance of GF-NG, we constructed a symmetrical supercapacitor by using two pieces of GF-NG with the same size and weight (insets of Figure 4f and Figure S15b, Supporting Information), tested in 6.0 M KOH electrolyte. As shown in Figure 4a and Figure S15a (Supporting Information), the CV curves show quasi-rectangular shapes, and no redox peak appears even at a high scan rate. Such typical behavior of electrical double-layer capacitor indicates the high rate capability and low internal resistance. With the scan rate increasing from 5 to 800 mV s⁻¹, the capacitance is still as high as 170 F g⁻¹ (Figure S15b, Supporting Information). The low internal resistance is essentially important for energy storage devices, because it means that less energy is wasted on producing undesirable heat during charging/discharging processes.^[49] We also measured the GCD at different current densities in the range of 0.3–80 A g⁻¹. As shown in Figure 4b, the GCD curves show symmetrical triangle with very small IR drop (Figure S16, Supporting Information) for each current density, indicating the reversible behavior of an ideal supercapacitor. At a current density of 0.3 A g⁻¹, the specific capacitance keeps at

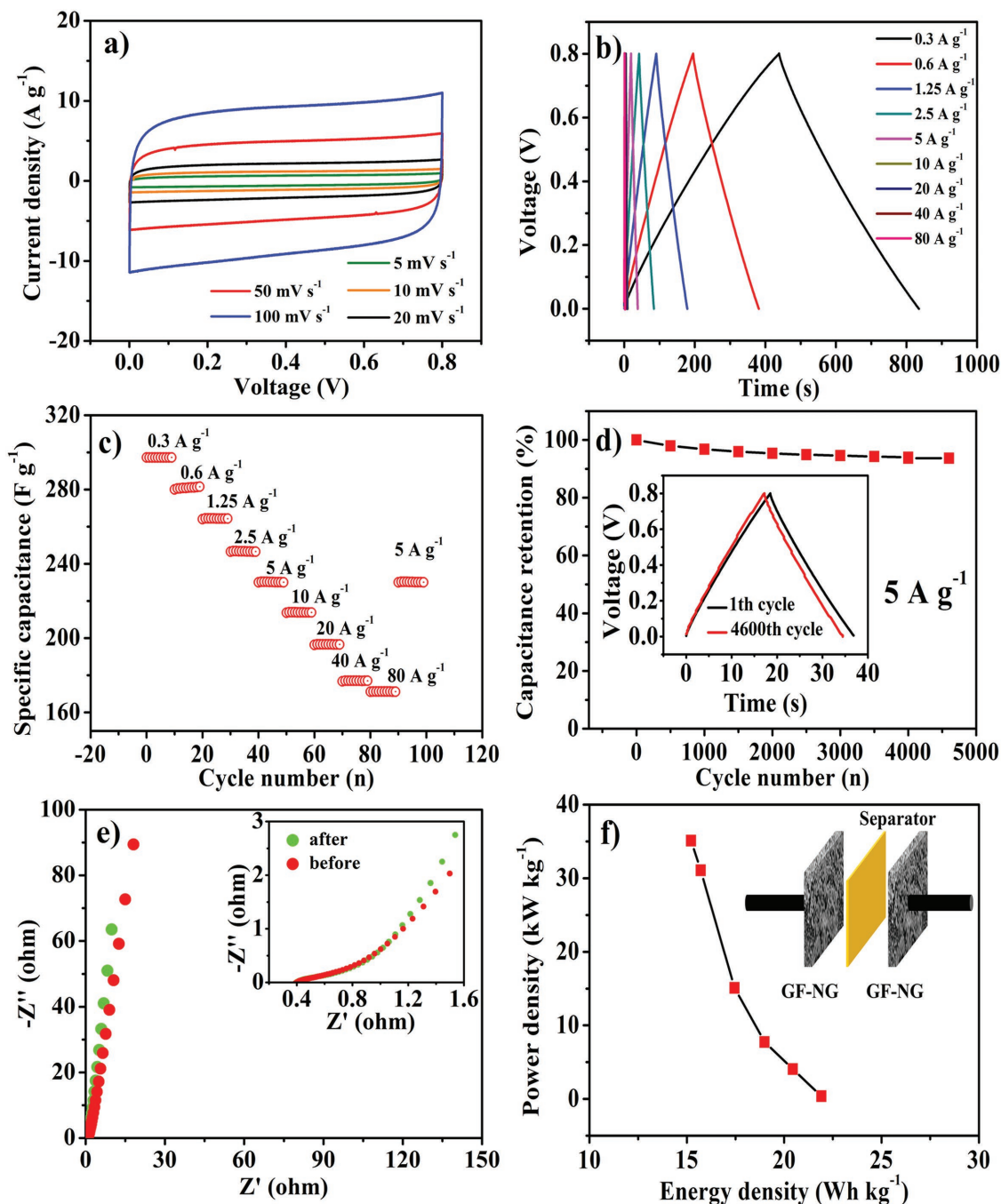


Figure 4. Electrochemical performances of GF-NG measured in two-electrode configuration in 6.0 M KOH. a) CV curves for scan rates from 5 to 100 mV s^{-1} for GF-NG. b) GCD curves under different constant currents. c) The specific capacitance calculated at various current densities of GF-NG (every current density is measured for nine segments). d) Cycling stability tests at a current density of 5 A g^{-1} . e) Nyquist plots of GF-NG and inset: the high-frequency region of the plot. f) Ragone plot of GF-NG and inset: schematic of symmetric two-electrode configuration.

297 F g^{-1} (Figure 4c), which is much higher than those of the NG deposited on nickel foam (223 F g^{-1}),^[3] ice-templated NG (217 F g^{-1}),^[37] and NG aerogel (223 F g^{-1}).^[50] Even at a high current density of 80 A g^{-1} , the specific capacitance still maintains at 171 F g^{-1} , showing the good stability of the electrode. More detailed comparisons are summarized in Table S2 (Supporting Information), which further confirm the advantages of our GF-NG over the reported porous materials for SCs.

A long cycle life is also a key factor for practical application of SCs. It was measured for 4600 times of charge/discharge at 5 A g^{-1} . After cycling, the capacitance (215 F g^{-1}) retains 93.5% of the initial value (230 F g^{-1} , Figure 4d). As mentioned above, the nitrogen atoms are uniformly distributed on the basal plane of graphene sheet, which are highly reversible and considerably stable during the cycling process, thus favoring the long-term electrochemical stability and excellent cycling

performance.^[29] It is known that both N-5 and N-6 can enhance the pseudocapacitance by involving into the redox process, and N-Q can promote the conductivity of graphene. Moreover, it was reported that during electrochemical test, (i) N-Q can be formed by the protonated N-6, which is feasible and irreversible, and (ii) the redox between N-5 and N-6 is reversible.^[48,51] Thus, we examined the nitrogen distribution after cycling tests by XPS (Figure S17, Supporting Information). It was found that (i) the nitrogen content shows a slight decrease (from 15.8 to 14.5 at%), and (ii) the N-5 content decreased, but the contents of both N-6 and N-Q increased. Moreover, the sum of the contents of N-5 and N-6 decrease from 88.7 to 82.3 at%, which is consistent with the attenuation of capacitance (6.5%). Therefore, we suggest that the drop of the capacitance may result from the two types of redox reactions (between N-5 and N-6, and N-6 to N-Q) during cycling.

Electrochemical impedance spectroscopy (EIS) is a key technique to be used to study the internal resistance of the electrode, as well as the resistance between the electrode and electrolyte. Figure 4e shows the Nyquist plots obtained from EIS in the frequency range of 0.01–100 kHz, and the inset is a magnified view of the curve in the high-frequency region. The appearance of the semicircle in the high-frequency region indicates that the GF-NG electrode has a very low charge transfer resistance and ion diffusion resistance. The equivalent series resistance (ESR) obtained from the first intersection with the real axis is only 0.4 Ω , further confirming a high charge transfer rate between the electrolyte and active materials with excellent conductive GF and NG. In the low-frequency region, the straight line represents the good capacitive behavior of the electrode and the more parallel to the virtual axis, the closer to the double-layer capacitance and the better the ion diffusion. It can be seen that the straight line is much closer to the virtual axis after cycles, revealing the improved ions diffusion behavior in the electrode. In general, the energy densities of PC-based SC devices based on an aqueous electrolyte are 3–5 Wh kg^{-1} and the power densities are less than 10 kW kg^{-1} (Table S2, Supporting Information).^[27,52] As reported,^[48] N-doping of graphene can contribute to both the high power and high energy density. As depicted in the Ragone plot (Figure 4f), the symmetric device based on our GF-NG aerogel hybrid networks delivers a maximum power density of 35.1 kW kg^{-1} at an energy density of 15.2 Wh kg^{-1} . Additionally, the electrochemical performances of GF-NG in both acidic and neutral electrolyte were tested. The specific capacitance, respectively, are 200 F g^{-1} in acidic electrolyte (Figure S18, Supporting Information) and 170 F g^{-1} in neutral electrolyte (Figure S19, Supporting Information), both of which are lower than the value of 297 F g^{-1} in alkaline electrolyte. We suggest that the low internal resistance and improved ion diffusion ability, together with the porous structure, large surface area, good wettability, and rich active sites by N-doping shown above, are responsible for the excellent performance of GF-NG for SCs.

In summary, the designed 3D GF-N-superdoped graphene hybrid networks exhibit significantly improved performance in SCs, which combine the high conductivity of GF skeletons, the enhanced wettability, and high N concentration of NG aerogels, and the large surface areas of both GF network and porous NG aerogels. The excellent capacitances can be up to 380, 332, and

245 F g^{-1} , respectively, in alkaline, acidic, and neutral electrolyte electrolytes measured in three-electrode configuration. In practical devices, the material can achieve remarkably high capacitance of 297 F g^{-1} , good cycling stability with 93.5% of the capacitance retention after 4600 cycles, and low internal resistance up to 0.4 Ω . We believe that the 3D GF-N-superdoped graphene network may be a promising material for the applications in catalysis, adsorption, energy storage, etc.

Experimental Section

Preparation of 3D GF-NG Networks: Graphene foam on nickel foam (NF/GF) was grown on NF (Changsha Liyuan New Material Co. Ltd., $\approx 350 \text{ g m}^{-2}$ in area density and $\approx 1.4 \text{ mm}$ in thickness) by CVD method.^[15] GO was prepared by modified Hummer's method.^[34] Then the GO solution was diluted to 6 mg mL^{-1} and ultrasonic treated for 30 min. After that, the NF/GF was immersed in GO aqueous dispersion treated for another 10 min ultrasonic treatment and kept at 60 $^{\circ}\text{C}$ for 24 h. The obtained NF/GF full of wet GO gels was suddenly frozen with liquid nitrogen, and freeze-dried for 24 h to obtain GO aerogels in the pores of NF/GF. After that, the sample was annealed in Ar atmosphere at 600 $^{\circ}\text{C}$ for 1 h to reduce the GO aerogels into rGO aerogels. Next, the sample was immersed in 1.0 M FeCl_3 and 1.0 M HCl solution for 24 h for etching the NF framework and repeatedly washed with purified water for several times. Subsequently, the wet GF-rGO material was subjected to another freeze-drying for 24 h to obtain 3D GF-rGO networks.^[36] GF-FG was obtained by annealing the mixture of GF-rGO and XeF_2 with the mass ratio of 1:20 in a sealed Teflon container at 200 $^{\circ}\text{C}$ for 20 h.^[53] After annealing GF-FG in ammonia at 500 $^{\circ}\text{C}$ for 1 h under ambient pressure, GF-NG network was obtained. When the mass ratio of GF-rGO to XeF_2 was changed to 1:10 and 1:5, the GF-NG-8.94 and GF-NG-5.46 with lower N-doping level were obtained. The GF-NG samples with lower mass loading of NG were synthesized by immersing NF into lower concentration of GO solutions.

Preparation of the Control Experiment of 3D GF Filled with NG Sheets: NG powder was diluted into the concentration (6 mg mL^{-1}) with deionized water and then ultrasonic treated for 30 min. After that, the GF was put into the NG solution and ultrasonic treated for 10 min. Then GF filled with NG sheets was obtained by immersing the GF into the NG solution at 60 $^{\circ}\text{C}$ for 24 h. Then it was suddenly frozen with liquid nitrogen, and freeze-dried for 24 h to obtain GF filled with NG sheets.

Preparation of 3D F-GF and N-GF Networks: F-GF was obtained by annealing the mixture of GF and XeF_2 with the mass ratio of 1:20 in a sealed Teflon container at 200 $^{\circ}\text{C}$ for 20 h. After annealing F-GF in ammonia at 500 $^{\circ}\text{C}$ for 1 h under ambient pressure, N-GF network was obtained.

Materials Characterization: FESEM and EDS measurements were performed using Oxford X-MAX 50, UK (15 kV). TEM measurement was examined using Model JEOL-2010, Japan. XPS measurements were performed on a PHI5000 VersaProbe (ULVAC-PHI, Japan) using 200 W monochromated Al $K\alpha$ radiation. A 500 μm X-ray spot was used for XPS analysis. The XPS peak fitting programme XPSPEAK 4.1 was used for the spectra processing. Raman spectra were obtained by a Raman system (Renishaw, England) using a 532 nm laser as the light source. Specific surface area was obtained by the Brunauer–Emmett–Teller (BET) calculation method, and pore size distributions were determined by the Barret–Joyner–Halenda (BJH) from N_2 adsorption–desorption isotherms measured by an accelerated surface area and porosimetry system (Micromeritics ASAP 2460, USA).

Electrochemical Performance Measurements: Two-electrode configurations tested in 6.0 M KOH aqueous solutions were used to evaluate the electrochemical performance. Two identical GF-NG sheets without binder or conductive additive (1.0 cm \times 1.0 cm each) were separated by a thick separator (NKK TF45, 40 μm) (Figure 4f and Figure S15b, Supporting Information). GF serves as the current collector and no binder existed. As for three-electrode configuration,

platinum foil and Ag/AgCl were used as the counter and reference electrodes, respectively. The electrolytes were 6.0 M KOH, 1.0 M H₂SO₄, and 1.0 M KCl aqueous solutions in three-electrode configuration. The performances of GF-NG were characterized by CV, GCD, and EIS on an electrochemical workstation (CHI 660D, Chenhua Instruments, China) for three-electrode configurations and blue electric system (battery testing system (LAND CT2001A)) for two-electrode tests. The calculations of the capacitances were followed by the equations displayed in the Supporting Information.

Supporting Information

Supporting Information is available from the Wiley Online Library or from the author.

Acknowledgements

The authors acknowledge financial support from MOST (Nos. 2014CB921102, 2014CB932402, and 2016YFA0200101), the National Science Foundation of China (51572122, 51325205, 51290273, and 51521091), "Strategic Priority Research Program" of the Chinese Academy of Sciences (XDA01020304), and Key Research Program of the Chinese Academy of Sciences (Nos. KGZD-EW-303-1 and KGZD-EW-T06).

Conflict of Interest

The authors declare no conflict of interest.

Keywords

electrochemical behaviors, graphene foams, highly conductive, nitrogen-superdoping, reduced graphene oxide

Received: March 25, 2017
Revised: May 15, 2017
Published online: July 24, 2017

- [1] P. Simon, Y. Gogotsi, *Nat. Mater.* **2008**, *7*, 10.
 [2] J. R. Miller, P. Simon, *Science* **2008**, *321*, 651.
 [3] H. F. Huang, C. L. Lei, G. S. Luo, Z. Z. Cheng, G. X. Li, S. L. Tang, Y. W. Du, *J. Mater. Sci.* **2016**, *51*, 6348.
 [4] J. Yan, Q. Wang, T. Wei, Z. J. Fan, *Adv. Energy Mater.* **2014**, *4*, 1300816.
 [5] J. Xu, Z. Tan, W. Zeng, G. Chen, S. Wu, Y. Zhao, K. Ni, Z. Tao, M. Ikram, H. Ji, Y. Zhu, *Adv. Mater.* **2016**, *28*, 5222.
 [6] J. Zhu, D. Yang, Z. Yin, Q. Yan, H. Zhang, *Small* **2014**, *10*, 3480.
 [7] X. Z. Zhou, Z. Y. Bai, M. J. Wu, J. L. Qiao, Z. W. Chen, *J. Mater. Chem. A* **2015**, *3*, 3343.
 [8] M. Jiang, L. B. Xing, J. L. Zhang, S. F. Hou, J. Zhou, W. Si, H. Cui, S. Zhuo, *Appl. Surf. Sci.* **2016**, *368*, 388.
 [9] Y. Xu, G. Shi, X. Duan, *Acc. Chem. Res.* **2015**, *48*, 1666.
 [10] C. Li, G. Shi, *Adv. Mater.* **2014**, *26*, 3992.
 [11] S. Mao, G. Lu, J. Chen, *Nanoscale* **2015**, *7*, 6924.
 [12] X. B. Liu, Z. P. Wu, Y. H. Yin, *Synth. Met.* **2017**, *223*, 145.
 [13] H. R. Naderia, P. Norouzia, R. M. Ganjaliala, *Appl. Surf. Sci.* **2016**, *366*, 552.
 [14] X. H. Cao, Z. Y. Yin, H. Zhang, *Energy Environ. Sci.* **2014**, *7*, 1850.
 [15] Z. Chen, W. Ren, L. Gao, B. Liu, S. Pei, H. M. Cheng, *Nat. Mater.* **2011**, *10*, 424.
 [16] W. Li, S. Gao, L. Wu, S. Qiu, Y. Guo, X. Geng, M. Chen, S. Liao, C. Zhu, Y. Gong, M. Long, J. Xu, X. Wei, M. Sun, L. Liu, *Sci. Rep.* **2013**, *3*, 2125.
 [17] S. Mao, Z. Wen, H. Kim, G. Lu, P. Hurley, J. Chen, *ACS Nano* **2012**, *6*, 7505.
 [18] X. H. Cao, Y. M. Shi, W. H. Shi, G. Lu, X. Huang, Q. Y. Yan, Q. C. Zhang, H. Zhang, *Small* **2011**, *7*, 3163.
 [19] H. S. Ahn, J. M. Kim, C. Park, J. W. Jang, J. S. Lee, H. Kim, M. Kaviani, M. H. Kim, *Sci. Rep.* **2013**, *3*, 1960.
 [20] S. Mao, K. Yu, J. Chang, D. A. Steeber, L. E. Ocola, J. Chen, *Sci. Rep.* **2013**, *3*, 1696.
 [21] D. Hulicova-Jurcakova, M. Kodama, S. Shiraiishi, H. Hatori, Z. H. Zhu, G. Q. Lu, *Adv. Funct. Mater.* **2009**, *19*, 1800.
 [22] X. I. Fan, X. I. Chen, L. M. Dai, *Curr. Opin. Colloid Interface Sci.* **2015**, *20*, 429.
 [23] L. Zhang, D. DeArmond, N. T. Alvarez, D. L. Zhao, T. T. Wang, G. F. Hou, R. Malik, W. R. Heineman, V. Shanov, *J. Mater. Chem. A* **2016**, *4*, 1876.
 [24] K. F. Chen, S. Y. Song, F. Liu, D. F. Xue, *Chem. Soc. Rev.* **2015**, *44*, 6230.
 [25] G. M. Zhou, L. Li, C. Q. Ma, S. G. Wang, Y. Shi, N. Koratkar, W. C. Ren, F. Li, H. M. Cheng, *Nano Energy* **2015**, *11*, 356.
 [26] J. Chen, K. Sheng, P. Luo, C. Li, G. Shi, *Adv. Mater.* **2012**, *24*, 4569.
 [27] Y. F. Deng, Y. Xie, K. X. Zou, X. L. Ji, *J. Mater. Chem. A* **2016**, *4*, 1144.
 [28] M. M. Fan, Z. Q. Feng, C. L. Zhu, X. Chen, C. T. Chen, J. Z. Yang, D. P. Sun, *J. Mater. Sci.* **2016**, *51*, 10323.
 [29] Z. Wen, X. Wang, S. Mao, Z. Bo, H. Kim, S. Cui, G. Lu, X. Feng, J. Chen, *Adv. Mater.* **2012**, *24*, 5610.
 [30] F. Y. Bana, S. Jayabala, H. N. Limb, H. W. Leec, N. M. Huang, *Ceram. Int.* **2017**, *43*, 20.
 [31] Y. X. Zhang, J. Zhang, D. S. Su, *ChemSusChem* **2014**, *7*, 1240.
 [32] G. H. Jun, S. H. Jin, B. Lee, B. H. Kim, W. S. Chae, S. H. Hong, S. Jeon, *Energy Environ. Sci.* **2013**, *6*, 3000.
 [33] C. N. R. Rao, K. Gopalakrishnan, A. Govindaraj, *Nano Today* **2014**, *9*, 324.
 [34] Y. Liu, Y. T. Shen, L. T. Sun, J. C. Li, C. Liu, W. C. Ren, F. Li, L. B. Gao, J. Chen, F. Liu, Y. Y. Sun, N. J. Tang, H. M. Cheng, Y. W. Du, *Nat. Commun.* **2016**, *7*, 10921.
 [35] L. M. Dai, *Nat. Energy* **2016**, *1*, 1.
 [36] G. J. Hu, C. Xu, Z. H. Sun, S. G. Wang, H. M. Cheng, F. Li, W. C. Ren, *Adv. Mater.* **2016**, *28*, 1603.
 [37] M. Kota, X. Yu, S. Yeon, H. Cheong, H. S. Park, *J. Power Sources* **2016**, *303*, 372.
 [38] S. B. Ye, J. C. Feng, P. Y. Wu, *ACS Appl. Mater. Interfaces* **2013**, *5*, 7122.
 [39] J. T. Xu, M. Wang, N. P. Wickramaratne, M. Jaroniec, S. X. Dou, L. M. Dai, *Adv. Mater.* **2015**, *27*, 2042.
 [40] S. Han, D. Q. Wu, S. Li, F. Zhang, X. L. Feng, *Adv. Mater.* **2014**, *26*, 849.
 [41] H. M. Jeong, J. W. Lee, W. H. Shin, Y. J. Choi, H. J. Shin, J. K. Kang, J. W. Choi, *Nano Lett.* **2011**, *11*, 2472.
 [42] X. W. Wang, *RSC Adv.* **2016**, *6*, 31359.
 [43] V. Singh, D. Joung, L. Zhai, S. Das, S. I. Khondaker, S. Seal, *Prog. Mater. Sci.* **2011**, *56*, 1178.
 [44] D. Hulicova-Jurcakova, M. Seredych, G. Q. Lu, T. J. Bandoz, *Adv. Funct. Mater.* **2009**, *19*, 438.
 [45] M. Seredych, D. Hulicova-Jurcakova, G. Q. Lu, T. J. Bandoz, *Carbon* **2008**, *46*, 1475.

- [46] L. Ma, R. Liu, H. Niu, L. Xing, L. Liu, Y. Huang, *ACS Appl. Surf. Sci.* **2016**, *8*, 33608.
- [47] O. Ornelas, J. M. Sieben, R. Ruiz-Rosas, E. Morallon, D. Cazorla-Amoros, J. Geng, N. Soin, E. Siores, B. F. Johnson, *Chem. Commun.* **2014**, *50*, 11343.
- [48] T. Q. Lin, I.-W. Chen, F. X. Liu, C. Y. Yang, B. Hui, F. F. Xu, F. Q. Huang, *Science* **2015**, *350*, 1508.
- [49] Q. Wu, Y. X. Xu, Z. Y. Yao, A. R. Liu, G. Q. Shi, *ACS Nano* **2010**, *4*, 8.
- [50] Z. Y. Sui, Y. N. Meng, P. W. Xiao, Z. Q. Zhao, Z. X. Wei, B. H. Han, *ACS Appl. Mater. Interfaces* **2015**, *7*, 1431.
- [51] D. W. Wang, F. Li, L. C. Yin, X. Lu, Z. G. Chen, I. R. Gentle, G. Q. Lu, H. M. Cheng, *Chem. Eur. J.* **2012**, *18*, 5345.
- [52] Y. Zhu, S. Murali, M. D. Stoller, K. J. Ganesh, W. Cai, P. J. Ferreira, A. Pirkle, R. M. Wallace, K. A. Cychosz, M. Thommes, D. Su, E. A. Stach, R. S. Ruoff, *Science* **2011**, *332*, 1537.
- [53] Q. Feng, N. J. Tang, F. C. Liu, Q. Q. Cao, W. H. Zheng, W. C. Ren, X. G. Wan, Y. W. Du, *ACS Nano* **2013**, *7*, 6729.